Fast image reconstruction for near-field terahertz imaging with multistatic non-uniform sparse arrays

Amir Masoud Molaei*[a], Shaoqing Hu[b], Vasiliki Skouroliakou[a], Vincent Fusco[a], Xiaodong Chen[c], Okan Yurduseven[a]

[a]Institute of Electronics, Communications and Information Technology (ECIT), Queen's University Belfast, Queen's Road, Belfast, U.K. BT3 9DT; [b]College of Engineering, Design and Physical Sciences, Brunel University London, Kingston Lane, Uxbridge, U.K. UB8 3PH; [c]School of Electrical Engineering and Computer Science, Queen Mary University of London, Mile End Road, London, U.K. E1 4NS

ABSTRACT

In this paper, first, the structure of a linear sparse periodic array for two-dimensional scanning is described. Then, based on its characteristics, an algorithm is presented for fast image reconstruction of the scene in a near-field (NF) multistatic terahertz imaging scenario. Although the basis of this algorithm is developed in the Fourier domain, it is compatible with the non-uniform structure of the array and also takes into account the phase deviations caused by multistatic imaging in NF. The performance of the proposed approach is evaluated with numerical data obtained from electromagnetic simulations in FEKO as well as experimental data. The results are discussed in terms of computational time on the central processing unit and graphics processing unit as well as the quality of the reconstructed image.

Keywords: Fast image reconstruction, multistatic non-uniform array, near-field, THz imaging

1. INTRODUCTION

In recent years, terahertz (THz) radar imaging, due to its unique properties, has been one of the technologies of interest in various fields (such as automotive, clinical and medical applications, food and agricultural industries, non-destructive testing, pharmaceutical and security screening) to solve real-world challenges [1-3]. The ability to penetrate a wide range of materials, no detectable damage to biological tissues, and high imaging resolution are the most prominent advantages of THz radiation [4-6].

The most basic way to create a two-dimensional (2D) active radar aperture is to use a transmitter-receiver (Tx-Rx) antenna pair in monostatic mode and capture the scene information through a mechanical raster scan [7, 8]. However, despite its simplicity, such a mechanism is not efficient in terms of the data acquisition rate. An alternative and common approach is to perform 1D scanning with a linear array [9, 10]. For scanning a large-scale scene while satisfying the Nyquist rate (which corresponds to inter-element spacing in terms of wavelength) [11, 12], monostatic arrays are not a good choice; because they will need a very large number of antenna elements. This problem is more acute for the THz band and makes the practical implementation of THz imaging in such a structure sometimes impossible [13].

Using some types of multiple-input multiple-output (MIMO) arrays is a suitable option to reduce the number of elements [14-16]. In particular, sparse periodic arrays (SPAs) with large inter-element spacing have recently been proposed for multistatic MIMO THz imaging systems [16-18]. However, the special multistatic structure of SPA is such that it is not possible to directly apply conventional fast Fourier transform (FT)-based image reconstruction techniques in the near-field (NF) [19, 20]. On the other hand, traditional non-Fourier techniques for scene image reconstruction, such as generalized synthetic aperture focusing technique (GSAFT) [17, 21], least-squares [22, 23] and matched filter [24, 25], have a very high computational time.

*a.molaei@qub.ac.uk; fax 44 28 9097 1702; pure.qub.ac.uk/en/persons/amir-masoud-molaei

Aiming to address the above, our focus in this paper is on the development of a computationally efficient algorithm for image reconstruction compatible with SPAs in a NF multistatic THz imaging scenario. First, the structure of inter-element spacing in SPA is investigated and it is explained how this structure may create incompatibilities with conventional fast Fourier-based image reconstruction techniques. Then, for the mentioned scenario, a solution based on FT with reduced dimensions adapted to the non-uniform spacing of the virtual array is presented. The efficiency of the proposed solution is evaluated with both numerical and experimental data.

The rest of this paper is organized as follows: in Section 2, the system model is presented; Section 3 details the proposed solution; Section 4 is devoted to the presentation of results and analyzes; Section 5 provides a brief conclusion.

2. SYSTEM MODEL

Figure 1 shows the general structure of an imaging system using a linear SPA in a multistatic structure. Without the loss of generality, it is assumed that the data related to the interaction of Tx-Rx elements are collected in the form of time-division multiplexing [26]. To synthesize a 2D aperture, the array moves vertically with uniform sampling steps d_y. The SPA introduced in [27, 28], consists of $N_T/2$ Tx antenna elements with uniform inter-element spacing $d_T/2$ on both sides of the array, and N_R Rx antenna elements with uniform inter-element spacing $d_R = N_T d_T/2$ located in the middle of the two Tx parts (see Figure 2). In general, Tx and Rx sensors may have a vertical offset d_{TR}; however, the presence or absence of such an offset does not affect the procedure of solving the problem.

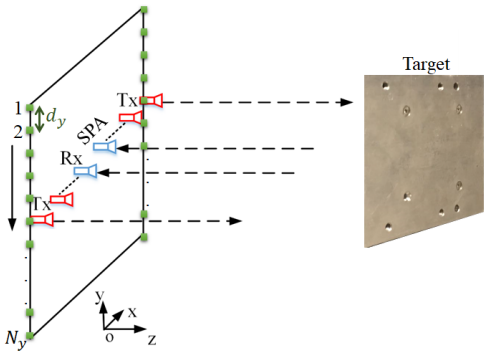

Figure 1. The general structure of the imaging system.

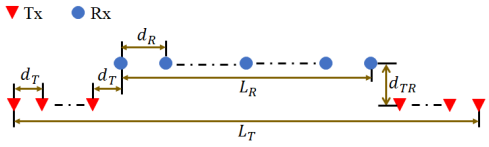

Figure 2. A display of the distribution of elements in SPA. $L_T = N_T d_T + (N_R - 1) d_R$ and $L_R = (N_R - 1) d_R$.

3. PROPOSED SOLUTION

Under the far-field (FF) assumption and using the effective phase center principle [9], the topology of the multistatic array in Figure 2 with $N_T + N_R$ physical antennas can be transformed into a denser linear virtual monostatic array with $N_T N_R$ elements in the form of Figure 3.

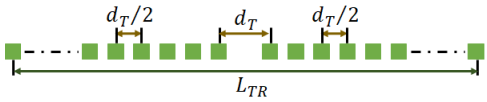

Figure 3. The virtual array corresponding to Figure 2 where $L_{TR} = (L_T + L_R)/2$.

Since in this paper, we are dealing with a NF scenario, the direct application of the above model lacks sufficient accuracy for the image reconstruction algorithm, and it is necessary to consider compensations for it. Multistatic-to-monostatic

conversion [29, 30] is an efficacious solution to adapt the multistatic data collected by the topology of Figure 2 to the monostatic model of Figure 3. Let $(x_C, y_C, 0)$ be the position of the phase center corresponding to the Tx and Rx elements in $(x_T, y_T, 0)$ and $(x_R, y_R, 0)$. The multistatic data set $s(x_T, y_T, x_R, y_R)$ can be converted to an effective monostatic version as follows:

$$\tilde{s}(x_C, y_C) = s(x_T, y_T, x_R, y_R) \frac{s_o(x_C, y_C)}{s_o(x_T, y_T, x_R, y_R)}, \tag{1}$$

where $s_o(x_C, y_C)$ and $s_o(x_T, y_T, x_R, y_R)$ represent monostatic and multistatic reference signals, respectively [29].

Due to the gap in the virtual array center (see Figure 3), data $\tilde{s}(x_C, y_C)$ is still not fully compatible with conventional Fourier-based image reconstruction techniques [18, 28]. In [28], the effect of this gap on the final results is shown, and to neutralize it, an additional phase interpolation step in the virtual array center is presented.

The following is a solution to reconstruct the image in the 1D Fourier domain (instead of the 2D Fourier domain), which, in addition to adapting to the imaging model in Figure 1, does not require the Stolt interpolation [31, 32] and phase interpolation. By considering (1) and using the first Born approximation [33], the backscattered data associated with a distributed target can be written as follows:

$$\tilde{s}(x_T, x_R, y_C) \simeq \int_x \int_y \sigma(x, y) e^{-j2k_0\sqrt{(x-x_C)^2+(y-y_C)^2+z_0^2}} dy dx, \tag{2}$$

where $\sigma(x, y)$ represents the 2D reflectivity of the target, z_0 denotes the target range, $k_0 = 2\pi f_0 / c$ is the wavenumber corresponding to the carrier frequency f_0, and c is the speed of light. By using the backpropagation imaging equation [28], the target image can be retrieved as

$$\sigma(x, y) \simeq \int_{x_T} \int_{x_R} \int_{y_C} \tilde{s}(x_T, x_R, y_C) e^{j2k_0\sqrt{(x-x_C)^2+(y-y_C)^2+z_0^2}} dy_C dx_R dx_T. \tag{3}$$

In the above equation, the inner integral can be considered as a convolution operation with respect to y. So, we have

$$\sigma(x, y) \simeq \int_{x_T} \int_{x_R} \tilde{s}(x_T, x_R, y) * e^{j2k_0\sqrt{(x-x_C)^2+y^2+z_0^2}} dx_R dx_T. \tag{4}$$

By taking the FT with respect to y from both sides of the above equation, we have

$$\varsigma(x, k_y) \simeq \int_{x_T} \int_{x_R} \tilde{S}(x_T, x_R, k_y) H(x, x_C, k_y) dx_R dx_T, \tag{5}$$

where $\varsigma(x, k_y)$, $\tilde{S}(x_T, x_R, k_y)$ and $H(x, x_C, k_y)$, respectively, represent the FT of $\sigma(x, y)$, $\tilde{s}(x_T, x_R, y)$ and $h(x, x_C, y) \triangleq e^{j2k_0\sqrt{(x-x_C)^2+y^2+z_0^2}}$ with respect to y. The above equation states that for each point x on the scene, the value of ς can be calculated by considering the data collected by all Txs and Rxs and their superposition. As a result, the target image can be obtained using the following closed-form expression:

$$\varsigma(x, y) \simeq \mathrm{FT}^{-1}_{1\mathrm{D},y} \left[\sum_{i=1}^{N_T} \int_{x_R} \mathrm{FT}_{1\mathrm{D},y} \left[\tilde{s}_i(x_R, y) \right] \mathrm{FT}_{1\mathrm{D},y} \left[h_i(x_m, x_C, y) \right] dx_R \right], \quad m = 1, 2, ..., M_x, \tag{6}$$

where $\tilde{s}_i$ and h_i represent the values of $\tilde{s}$ and h corresponding to the i-th Tx antenna, respectively, and M_x is the number of points defined to discretize x. In the above equation, the Tx and Rx components can be easily swapped, so that the outer summation is applied to Rx elements instead of Tx ones

$$\varsigma(x, y) \simeq \mathrm{FT}^{-1}_{1\mathrm{D},y} \left[\sum_{i'=1}^{N_R} \int_{x_T} \mathrm{FT}_{1\mathrm{D},y} \left[\tilde{s}_{i'}(x_T, y) \right] \mathrm{FT}_{1\mathrm{D},y} \left[h_{i'}(x_m, x_C, y) \right] dx_T \right], \quad m = 1, 2, ..., M_x, \tag{7}$$

where $\tilde{s}_{i'}$ and $h_{i'}$ represent the values of $\tilde{s}$ and h corresponding to the i'-th Rx antenna, respectively.

4. RESULTS AND DISCUSSION

In this section, simulation results based on numerical electromagnetic data and experimental data are given. For the studies presented in this section, all computations were done on MATLAB R2021b of 64-bit Windows Server 2019 operating system with 128 GB of random-access memory, a Core-i9 central processing unit (CPU) at 2.8 GHz, and a NVIDIA Quadro RTX 5000 graphics processing unit (GPU) with 16 GB memory. The reconstructed images by the proposed solution are compared with those of the generalized synthetic aperture focusing technique (GSAFT) [17, 21]. Also, the computational time of these methods in CPU and GPU are compared and discussed. The target profiles are shown in Figures 4(a) and 4(b). The first is a rectangular metal plate with a size of $145\times120\times5\,\text{mm}^3$. The metal plate has several holes of different diameters (see Figure 4(a)). The second is a pure metallic target in which the sizes of the rectangular holes are 3×5, 5×7, 7×10 and $10\times15\,\text{mm}^2$, respectively, from small to large (see Figure 4 (b)). The sizes of large squares and the squares inside them are 30×30 and $10\times10\,\text{mm}^2$, respectively. In all examples, the number of points defined to discretize y is fixed and equal to $M_y=128$. Computational times are obtained based on averaging from 20 independent runs.

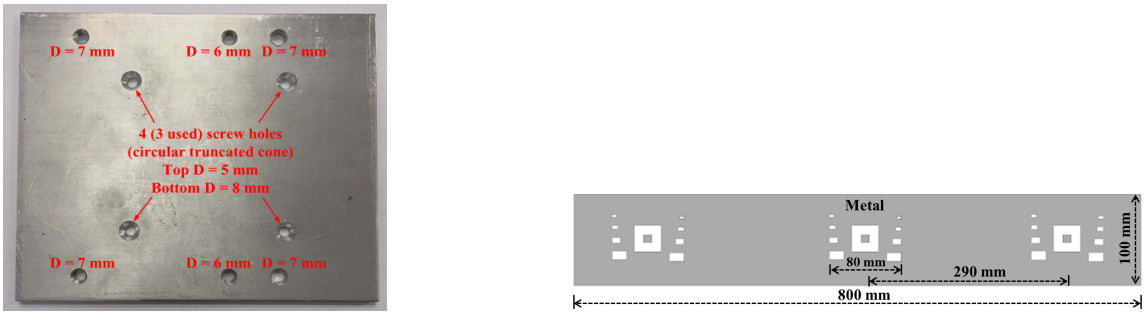

(a) (b)

Figure 4. A display of targets; (a) target profile 1 [34], (b) target profile 2.

The values of imaging system parameters related to target profile 1 are given in Table 1, where λ is the wavelength. According to the size of the virtual aperture, i.e. 192 mm (based on the parameter values in Table 1), and according to the operating frequency, targets with a range of less than approximately 54 m are located in the NF [35]. Figure 5 shows the images reconstructed by the proposed solution applied to the data obtained from electromagnetic simulations by FEKO [34, 36]. Also, in Table 2, the corresponding computational times for image reconstruction are given. The points that can be found from Figure 5 and Table 2 are given below. First, applying the superposition on Txs or Rxs (that is, applying (6) or (7) respectively) did not affect the outputs; in other words, both (6) and (7) work correctly. Second, since in this example, the number of Txs and Rxs are equal, the computational time for them is not different. Thirdly, in (6) or (7), it is obvious that the larger M_x is chosen, the better the reconstructed image quality may be expected. This comes at the cost of increased computation. This is consistent with the results. Fourthly, it can be concluded analytically from (6) or (7) and numerically from the results that the proposed solution is suitable for parallelizing and accelerating calculations by GPU. In fact, (6) (or (7)) indicates that the outer sum has an independent variable i (or i') that the operation corresponding to it can be performed as independent units in the GPU. Also, the findings of Table 2 show that the time spent on computing significantly exceeds the time spent on transferring data to and from the GPU memory (data transfer overhead). In this example, the speedup rate (by using GPU instead of CPU) when M_x is equal to 101 and 201 is 2.93 and 5.15, respectively. Note that in general, the more intensive the computations, the more noticeable the acceleration by the GPU compared to the CPU.

Table 1. Values of imaging system parameters related to target profile 1.

Parameter	f_0	N_T	N_R	N_y	d_T	d_R	d_{TR}	d_y	z_0
Value	220 GHz	8	8	76	6 mm (4.4λ)	24 mm (17.6λ)	0 mm	4 mm	1.1 m

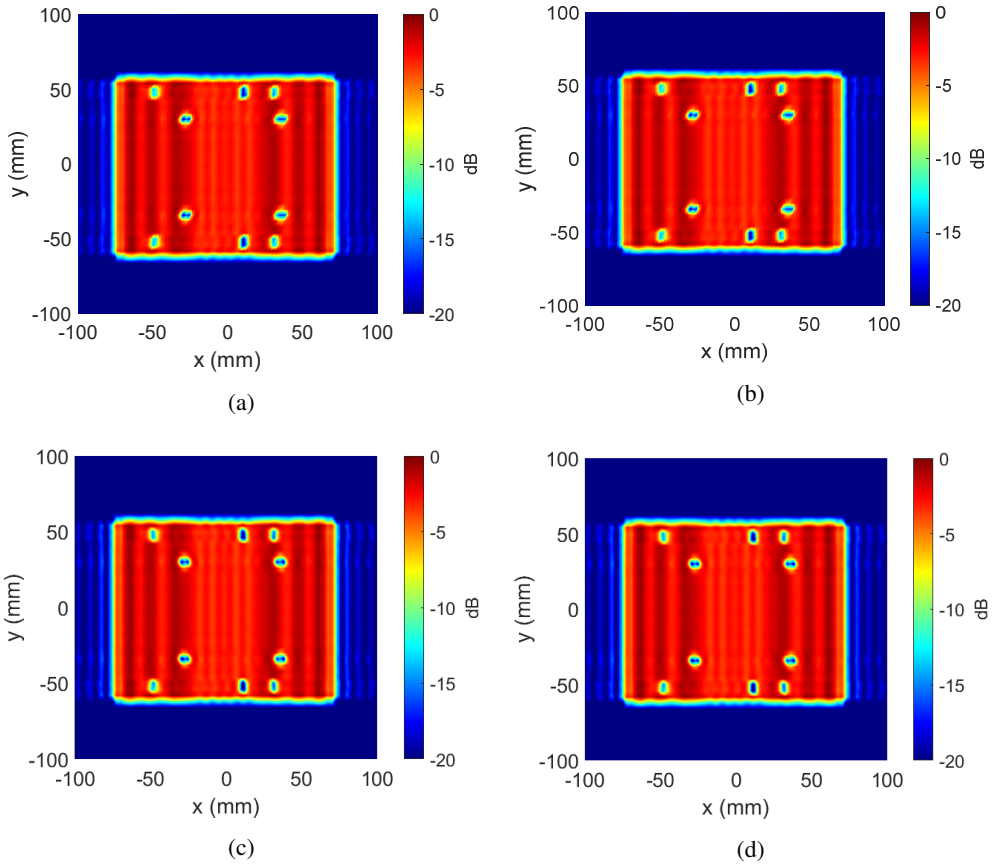

Figure 5. Images reconstructed by the proposed solution applied to data obtained from electromagnetic simulations; (a) employing (6), $M_x = 101$, (b) employing (7), $M_x = 101$, (c) employing (6), $M_x = 201$, (d) employing (7), $M_x = 201$.

Table 2. Computational times of reconstruction of images corresponding to Figure 5.

Figure	Processor	Computational Time (Sec)
5(a) and 5(b)	CPU	0.0164
5(a) and 5(b)	GPU (including overhead)	0.0056
5(a) and 5(b)	GPU (excluding overhead)	0.0055
5(c) and 5(d)	CPU	0.0314
5(c) and 5(d)	GPU (including overhead)	0.0061
5(c) and 5(d)	GPU (excluding overhead)	0.0059

To further verify the performance of the proposed solution, it was also evaluated using experimental data obtained in an anechoic test environment. The main parameters of the imaging system are the same values as in Table 1 (except that $d_{TR} = 181\,\text{mm}$ and $z_0 = 1.4\,\text{m}$). More details about the system setup (along with related photos) and how to collect the raw data are given in Section IV of [28]. The reconstructed images by the proposed solution and GSAFT are shown in Figure 6. Also, the corresponding computational times are given in Table 3. Consistent with previous studies [16, 37], GSAFT has provided relatively better resolution than a Fourier-based approach (compare the images of holes made in the target). However, computationally, in CPU and GPU, the proposed solution in this example has been 59.22 and 53.72

times faster than GSAFT, respectively. In addition, the speedup rate due to the use of GPU instead of CPU in GSAFT and the proposed solution is 5.67 and 5.15, respectively.

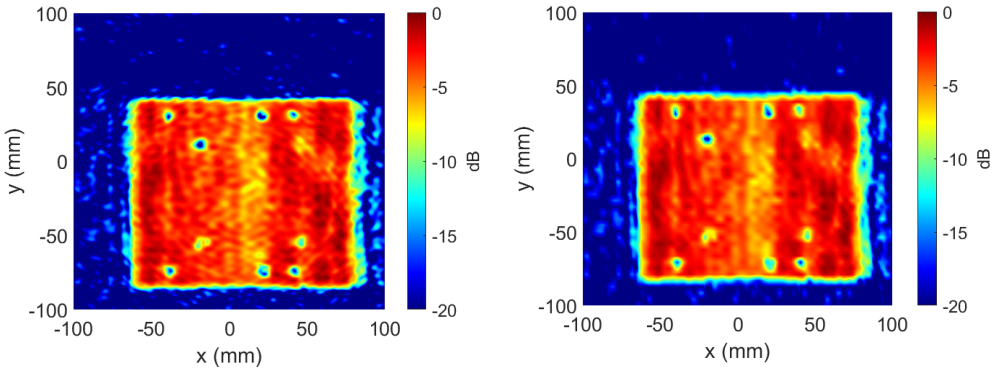

(a) (b)

Figure 6. Reconstructed images using experimental data; (a) by GSAFT, (b) by the proposed solution employing (6). $M_x = 201$.

Table 3. Computational times of reconstruction of images corresponding to Figure 6.

Figure	Processor	Computational Time (Sec)
6(a)	CPU	1.8595
6(a)	GPU (including overhead)	0.3277
6(b)	CPU	0.0314
6(b)	GPU (including overhead)	0.0061

In the last example, target profile 2 with a different aperture size is considered. The values of imaging system parameters are given in Table 4. The reconstructed images and the corresponding processing times are shown in Figure 7 and Table 5, respectively. By comparing the images in Figure 7, the following conclusions can be drawn. First, the increase in the number of pixels has led to the improvement of the quality of the images, so that even the smallest holes in the target can be identified in the images of the right column. Second, GSAFT outputs still provide slightly better resolution than the corresponding outputs of the proposed solution. Thirdly, using (6) or (7), despite the difference in the number of Tx and Rx antennas in this example, still did not affect the image output. The information in Table 5 shows that the proposed Fourier-based solution works much faster than GSAFT both on CPU and GPU. Note that computation times labeled GPU are provided with data transfer overhead included. However, this overhead is much smaller than the main signal processing time on the GPU and can be ignored (it is about 0.2 and 1 ms for $M_x = 101$ and $M_x = 301$, respectively). Also, the findings of Table 5 indicate that in this example, applying (7) is slightly more efficient than (6) in terms of calculations. This is due to the greater number of Rx antennas than Tx antennas. The speedup rate due to the use of GPU instead of CPU when applying (6) and (7) with $M_x = 101$ is 4.92 and 4.94, respectively, and with $M_x = 301$ is 10.45 and 11.36, respectively. These rates are 6.07 and 14.41 for GSAFT outputs for $M_x = 101$ and $M_x = 301$, respectively. It can be seen, as mentioned before, in general, the more intensive the computations (due to the increase in the amount of parameters involved in parallelization), the greater the benefit of using GPU. As the last quantitative comparison in this example, if we consider the information obtained from applying (7) in the proposed solution, in CPU, the processing speed of the proposed solution for $M_x = 101$ and $M_x = 301$ respectively shows 90.72 and 93.6 times improvement compared to GSAFT. These rates are 73.91 and 73.8 respectively in GPU.

5. CONCLUSION

In this paper, a fast Fourier-based solution compatible with the SPA structure was developed for NF multistatic THz imaging. The performance of the proposed solution was evaluated using both simulated electromagnetic data and

experimental data. The results of the experiments with two different target profiles and three different groups of parameters showed that despite the significant acceleration of the processes by the proposed approach, the reconstructed images have satisfactory quality. In addition, it was shown analytically and numerically that the proposed solution is compatible with the parallelization purposes in GPU. The achievements of this work can be promising for real-time imaging applications.

Table 4. Values of imaging system parameters related to target profile 2.

Parameter	f_0	N_T	N_R	N_y	d_T	d_R	d_{TR}	d_y	z_0
Value	220 GHz	14	16	81	7 mm (5.13λ)	49 mm (35.93λ)	0 mm	6 mm	4 m

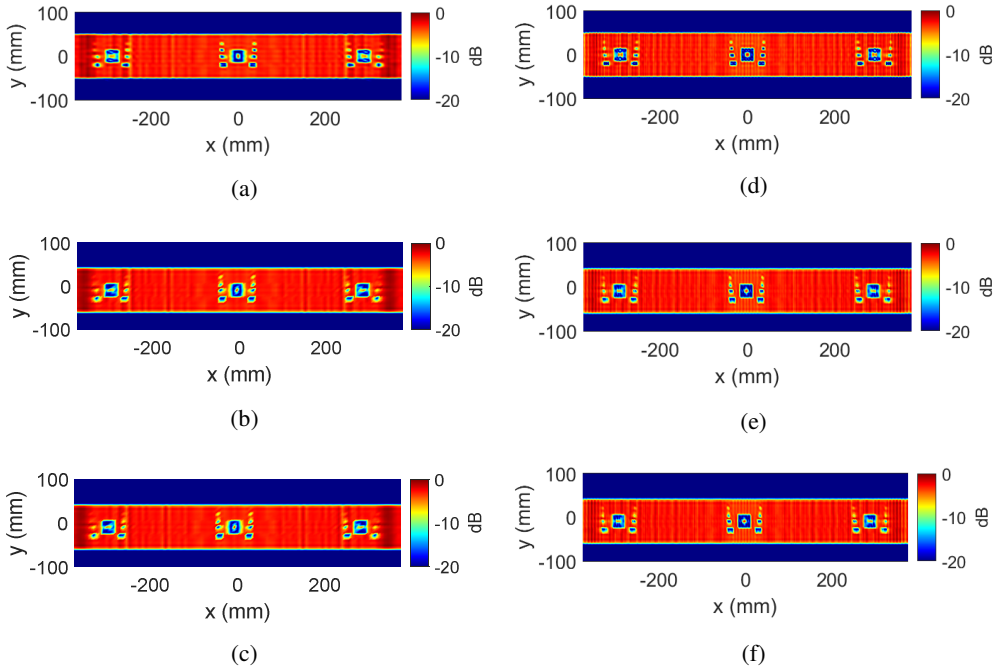

Figure 7. Images reconstructed using data obtained from electromagnetic simulations; (a) by GSAFT, $M_x = 101$, (b) by proposed solution employing (6), $M_x = 101$, (c) by proposed solution employing (7), $M_x = 101$, (d) by GSAFT, $M_x = 301$, (e) by proposed solution employing (6), $M_x = 301$, (f) by proposed solution employing (7), $M_x = 301$.

Table 5. Computational times of reconstruction of images corresponding to Figure 7.

Figure	Processor	Computational Time (Sec)	Figure	Processor	Computational Time (Sec)
7(a)	CPU	3.9916	7(d)	CPU	11.6995
7(a)	GPU	0.6578	7(d)	GPU	0.8118
7(b)	CPU	0.0433	7(e)	CPU	0.115
7(b)	GPU	0.0088	7(e)	GPU	0.011
7(c)	CPU	0.0440	7(f)	CPU	0.125
7(c)	GPU	0.0089	7(f)	GPU	0.011

ACKNOWLEDGMENT

This work was funded by the Leverhulme Trust under Research Leadership Award RL-2019-019. The work of Shaoqing Hu is funded by Brunel University London under Research Development Fund LBG194 and 2022/2023 Brunel Research Initiative and Enterprise Fund 12455.

REFERENCES

[1] D. Jasteh, E. G. Hoare, M. Cherniakov, and M. Gashinova, "Experimental low-terahertz radar image analysis for automotive terrain sensing," *IEEE Geoscience and Remote Sensing Letters,* vol. 13, no. 4, pp. 490-494, 2016.

[2] P. Hillger, J. Grzyb, R. Jain, and U. R. Pfeiffer, "Terahertz imaging and sensing applications with silicon-based technologies," *IEEE Transactions on Terahertz Science and Technology,* vol. 9, no. 1, pp. 1-19, 2018.

[3] C. Yingwu *et al.*, "Experimental research on high resolution terahertz radar imaging," *High Power Laser and Particle Beams,* vol. 24, no. 01, pp. 7-9, 2012.

[4] S. Ergün and S. Sönmez, "Terahertz technology for military applications," *Journal of Management and Information Science,* vol. 3, no. 1, pp. 13-16, 2015.

[5] X. Yang *et al.*, "Biomedical applications of terahertz spectroscopy and imaging," *Trends in biotechnology,* vol. 34, no. 10, pp. 810-824, 2016.

[6] L. Yu *et al.*, "The medical application of terahertz technology in non-invasive detection of cells and tissues: opportunities and challenges," *RSC advances,* vol. 9, no. 17, pp. 9354-9363, 2019.

[7] G. Kaur and A. Kaur, "Monostatic radar-based microwave imaging of breast tumor detection using a compact cubical dielectric resonator antenna," *Microwave and Optical Technology Letters,* vol. 63, no. 1, pp. 196-204, 2021.

[8] A. M. Molaei, R. Kumar, S. Hu, V. Skouroliakou, V. Fusco, and O. Yurduseven, "A compressive sensing-based approach for millimeter-wave imaging compatible with Fourier-based image reconstruction techniques," in *2022 23rd International Radar Symposium (IRS)*, 2022: IEEE, pp. 87-91.

[9] A. M. Molaei, S. Hu, V. Fusco, and O. Yurduseven, "A multi-resolution analysis-based approach to accelerate data acquisition for near-field MIMO millimeter-wave imaging," in *Passive and Active Millimeter-Wave Imaging XXV*, 2022, vol. 12111: SPIE, pp. 90-101.

[10] A. M. Molaei, O. Yurduseven, and V. Fusco, "An efficient waveform diversity based on variational mode decomposition of coded beat-frequency shifted signals algorithm for multiple-input multiple-output millimetre-wave imaging," *IET Radar, Sonar & Navigation,* vol. 15, no. 10, pp. 1266-1280, 2021.

[11] X. Liu, T. Wei, C. Sun, Y. Yang, and J. Zhuo, "High-resolution two-dimensional imaging using MIMO sonar with limited physical size," *Applied Acoustics,* vol. 182, p. 108280, 2021.

[12] T. Gong *et al.*, "Holographic MIMO Communications: Theoretical Foundations, Enabling Technologies, and Future Directions," *arXiv preprint arXiv:2212.01257,* 2022.

[13] A. M. Molaei, S. Hu, V. Skouroliakou, V. Fusco, X. Chen, and O. Yurduseven, "Fourier compatible near-field multiple-input multiple-output terahertz imaging with sparse non-uniform apertures," *IEEE Access,* vol. 9, pp. 157278-157294, 2021.

[14] A. M. Molaei, P. del Hougne, V. Fusco, and O. Yurduseven, "Efficient joint estimation of DOA, range and reflectivity in near-field by using mixed-order statistics and a symmetric MIMO array," *IEEE Transactions on Vehicular Technology,* vol. 71, no. 3, pp. 2824-2842, 2021.

[15] I. Ishteyaq and K. Muzaffar, "Multiple input multiple output (MIMO) and fifth generation (5G): An indispensable technology for sub-6 GHz and millimeter wave future generation mobile terminal applications," *International Journal of Microwave and Wireless Technologies,* vol. 14, no. 7, pp. 932-948, 2022.

[16] S. Hu, A. M. Molaei, and O. Yurduseven, "220 GHz sparse imaging with multi-static aperiodic array," in *Passive and Active Millimeter-Wave Imaging XXV*, 2022, vol. 12111: SPIE, pp. 83-89.

[17] S. Hu *et al.*, "Multistatic MIMO Sparse Imaging Based on FFT and Low-Rank Matrix Recovery Techniques," *IEEE Transactions on Microwave Theory and Techniques,* vol. 71, no. 3, pp. 1285-1295, 2022.

[18] S. Hu, A. M. Molaei, and O. Yurduseven, "FFT-based 220 GHz Sparse Imaging for Target Detection," in *2022 International Workshop on Antenna Technology (iWAT)*, 2022: IEEE, pp. 76-78.

[19] A. M. Molaei, V. Skouroliakou, V. Fusco, and O. Yurduseven, "Efficient 3D image reconstruction for near-field microwave imaging using dynamic metasurface antenna," *IEEE Access,* vol. 10, pp. 68491-68498, 2022.

[20] A. M. Molaei, S. Hu, R. Kumar, and O. Yurduseven, "MIMO Coded Generalized Reduced Dimension Fourier Algorithm for 3-D Microwave Imaging," *IEEE Transactions on Geoscience and Remote Sensing,* vol. 61, 2023.
[21] F. Sepehripour, A. S. Alavijeh, M. Fakharzadeh, and A. Khavasi, "A broadband and compact millimeter-wave imaging system based on synthetic aperture radar," *arXiv preprint arXiv:2205.14707,* 2022.
[22] M. Ndoye, J. M. Anderson, and D. J. Greene, "An MM-Based Algorithm for ℓ1 -Regularized Least-Squares Estimation With an Application to Ground Penetrating Radar Image Reconstruction," *IEEE Transactions on Image Processing,* vol. 25, no. 5, pp. 2206-2221, 2016.
[23] J. Yin, K. P. Papathanassiou, J. Yang, and P. Chen, "Least-squares estimation for pseudo quad-pol image reconstruction from linear compact polarimetric SAR," *IEEE Journal of Selected Topics in Applied Earth Observations and Remote Sensing,* vol. 12, no. 10, pp. 3746-3758, 2019.
[24] E. O'Mahoney and I. Murray, "Evaluation of a matched filter resolution recovery reconstruction algorithm for SPECT-CT imaging," *Nuclear medicine communications,* vol. 34, no. 3, pp. 240-248, 2013.
[25] S. Devadithya, A. Pedross-Engel, C. M. Watts, and M. S. Reynolds, "Partitioned inverse image reconstruction for millimeter-wave SAR imaging," in *2017 IEEE International Conference on Acoustics, Speech and Signal Processing (ICASSP)*, 2017: IEEE, pp. 6060-6064.
[26] J. W. Smith and M. Torlak, "Efficient 3-D near-field MIMO-SAR imaging for irregular scanning geometries," *IEEE Access,* vol. 10, pp. 10283-10294, 2022.
[27] S. Hu, C. Shu, Y. Alfadhl, and X. Chen, "Advanced thz mimo sparse imaging scheme using multipass synthetic aperture focusing and low-rank matrix completion techniques," *IEEE Transactions on Microwave Theory and Techniques,* vol. 70, no. 1, pp. 659-669, 2021.
[28] A. M. Molaei, S. Hu, V. Skouroliakou, V. Fusco, X. Chen, and O. Yurduseven, "Fast processing approach for near-field terahertz imaging with linear sparse periodic array," *IEEE Sensors Journal,* vol. 22, no. 5, pp. 4410-4424, 2022.
[29] V. Skouroliakou, A. M. Molaei, V. Fusco, and O. Yurduseven, "Fourier-based radar processing for multistatic millimetre-wave imaging with sparse apertures," in *2022 16th European Conference on Antennas and Propagation (EuCAP)*, 2022: IEEE, pp. 1-5.
[30] V. Skouroliakou, A. M. Molaei, M. García-Fernández, G. Álvarez-Narciandi, and O. Yurduseven, "Frequency Domain Image Reconstruction for Imaging With Multistatic Dynamic Metasurface Antennas," *IEEE Access,* vol. 10, pp. 124728-124737, 2022.
[31] S. Jiacheng and M. Chen, "Research on imaging algorithm of millimeter wave radar based on stolt interpolation," in *2019 IEEE MTT-S International Microwave Biomedical Conference (IMBioC)*, 2019, vol. 1: IEEE, pp. 1-4.
[32] A. M. Molaei *et al.*, "Development of fast Fourier-compatible image reconstruction for 3D near-field bistatic microwave imaging with dynamic metasurface antennas," *IEEE Transactions on Vehicular Technology,* vol. 71, no. 12, pp. 13077-13090, 2022.
[33] Y. FAN, X. LI, Z. QI, and K. LU, "Second-order Born approximation imaging algorithm for transient electromagnetic pseudo wave-field," *Chinese Journal of Geophysics,* vol. 65, no. 3, pp. 1144-1159, 2022.
[34] S. Hu, C. Shu, Y. Alfadhl, and X. Chen, "A THz imaging system using linear sparse periodic array," *IEEE Sensors Journal,* vol. 20, no. 6, pp. 3285-3292, 2019.
[35] A. M. Molaei, P. Del Hougne, V. Fusco, and O. Yurduseven, "Numerical-Analytical Study of Performance of Mixed-Order Statistics Algorithm for Joint Estimation of DOA, Range and Backscatter Coefficient in a MIMO Structure," in *2022 23rd International Radar Symposium (IRS)*, 2022: IEEE, pp. 396-401.
[36] S. Hu, "Study on THz imaging system for concealed threats detection," *School of Electronic Engineering and Computer Science Queen Mary, University,* 2020.
[37] A. M. Molaei, T. Fromenteze, S. Hu, V. Fusco, and O. Yurduseven, "Fourier-Based Near-Field Three-Dimensional Image Reconstruction in a Multistatic Imaging Structure Using Dynamic Metasurface Antennas," *IEEE Transactions on Computational Imaging,* vol. 8, pp. 1089-1100, 2022.